Modelling and Simulation in
Materials Science and Engineering

PAPER • **OPEN ACCESS**

Polycrystalline silicon, a molecular dynamics study: II. Grains, grain boundaries and their structure

To cite this article: Antti Lahti *et al* 2024 *Modelling Simul. Mater. Sci. Eng.* **32** 065026

OPEN ACCESS
IOP Publishing
Modelling and Simulation in Materials Science and Engineering

Modelling Simul. Mater. Sci. Eng. **32** (2024) 065026 (22pp)
https://doi.org/10.1088/1361-651X/ad5dd3

Polycrystalline silicon, a molecular dynamics study: II. Grains, grain boundaries and their structure

Antti Lahti[1,*], Mikael Santonen[1], Zahra Jahanshah Rad[1], Mikko Miettinen[1], Masoud Ebrahimzadeh[1], Juha-Pekka Lehtiö[1], Pekka Laukkanen[1], Marko Punkkinen[1], Petriina Paturi[1], Kalevi Kokko[1], Antti Kuronen[2], Wei Li[3], Levente Vitos[3,4], Katja Parkkinen[5] and Markus Eklund[5]

[1] Department of Physics and Astronomy, University of Turku, FI-20014 Turku, Finland
[2] Department of Physics, University of Helsinki, PO Box 43, FI-00014 Helsinki, Finland
[3] Department of Physics and Astronomy, Division of Materials Theory, Uppsala University, Box 516, SE-751 20 Uppsala, Sweden
[4] Research Institute for Solid State Physics and Optics, Wigner Research Center for Physics, Budapest H-1525, Hungary
[5] Okmetic Oyj, PL 44, 01301 Vantaa, Finland

E-mail: ailaht@utu.fi

Received 31 January 2024; revised 20 May 2024
Accepted for publication 2 July 2024
Published 26 July 2024

Abstract

Polycrystalline silicon (poly-Si) is an excellent material for use in microelectronic devices, both in electrical and mechanical applications. Its mechanical and electrical properties are widely adjustable, its processing technology is compatible with existing microcircuit manufacturing technology, and its availability and recyclability are at a high level. Here, we focus on investigating the properties of poly-Si that distinguish it from other forms of silicon, that is, grains, grain boundaries, and the conditions and treatments that determine grain and grain boundary properties. Starting from the molecular dynamics simulations of the deposition of thin poly-Si films under different growth conditions

---

[*] Author to whom any correspondence should be addressed.

we study the properties of the films, grains, and grain boundaries as a function of growth time, growth temperature, and post-annealing. We aim to get data and information that will form the essential basis for future research on the electrical properties of poly-Si. The main results are: (i) the effect of post-annealing on the distribution of the grain size and grain boundary thickness (ii) the distribution of the grain orientations, and (iii) the density of the 3- and 5-bonded atoms as a function of deposition temperature.

Keywords: polycrystalline silicon, grain analysis, polycrystal growth

1. Introduction

Polycrystalline silicon (poly-Si) is a versatile material because it inherently has properties similar to single crystal silicon (c-Si) and amorphous silicon (a-Si). In addition to the traditional impurity doping, the properties of poly-Si can also be adjusted by modifying its grains and grain boundaries. In this work, we focus on grains, grain boundaries, and the treatments and conditions that affect their properties. We solve the distribution of the crystal directions of the grains in thin poly-Si films and we consider the possible reasons why some crystal directions are more likely than others. Also, we solve the distribution and structure of 3- and 5-coordinated atoms in poly-Si films deposited at temperatures 700 K, 800 K, and 900 K. The obtained data and information about miscoordinated atoms are useful to better understand how poly-Si reduces, in high-frequency electronic devices, harmful effects, such as loss, crosstalk, and non-linearity [1]. Miscoordinated Si atoms in poly-Si produce usually localised electronic states in the energy band gap of Si [2–6]. These band gap states can trap mobile electrons and holes and reduce the so-called harmful parasitic surface conductivity. The parasitic surface conductivity typically degrades the performance of otherwise high-quality radio-frequency (RF) devices. The reduction of loss, crosstalk, and nonlinearity depends largely on the detailed atomic structure of the grain boundaries, which in turn depends on the poly-Si growth parameters and post-treatments [7]. The present study is the second part of a series of studies of poly-Si (Part I [8] deals with the deposition of poly-Si).

Due to the complex structure of poly-Si, its research is quite challenging. However, due to its sustainable production and versatile application possibilities, interest in studying its properties has been quite extensive, both experimentally and theoretically. As an example of poly-Si studies, related to our work, we list some recent studies below.

Ding *et al* [9] reported, based on transmission electron microscopy (TEM) investigations, that the poly-Si/Si interface is the main factor controlling the electrical resistivity of the poly-Si films. Resistivity is strongly promoted by the $\Sigma3$ twin-type interface with a huge amount of extended defects. Interfaces with random characters do not favour the formation of such defects, leading to poor electrical resistivity.

Stokkan *et al* [10] studied fractions of different grain boundary types and the relationship between grain boundaries and dislocations. They used a scanning electron microscope (SEM) with electron backscatter diffraction (EBSD) in their investigations. EBSD was also used by Ratanaphan *et al* [11] to measure the grain boundary character distribution specifying the relative areas of grain boundaries as a function of lattice misorientation and grain boundary plane orientation.

Atomic force microscopy (AFM) was used by Mates [12] to reconstruct a cross-sectional shape of the poly-Si grain. Rumler *et al* [13] used AFM to characterise grain boundaries of poly-Si with high lateral resolution.

Grazing incidence x-ray diffraction (GIXRD) was used by Orapunt *et al* [14] to study amorphous-to-crystalline phase transition in Si-films. Raman spectroscopy was used to determine the crystalline volume fractions.

The structure of poly-Si has also been studied theoretically. Computational studies range from *ab initio* calculations to macroscopic modelling. Zhao and Li [15] investigated phosphorous (P) and arsenic (As) segregation at grain boundaries by using Vienna *Ab initio* Simulation Package (VASP). Deringer *et al* [16] showed that accurate structural models of a-Si can be obtained using a machine-learning-based interatomic potential, they generated a 4096-atom system that correctly reproduces the magnitude of the first sharp diffraction peaks in the structure factor. The potential was generated using, among other things, the Gaussian approximation potential (GAP) framework and the Smooth Overlap of Atomic Positions (SOAP).

The poly-Si films analysed in the present work have been produced in our previous work [8] using the Large-scale Atomic/Molecular Massively Parallel Simulator (LAMMPS) molecular dynamics simulator [17]. In these simulations, poly-Si was grown on top of amorphic silicon by depositing silicon atoms. For interatomic potential, we used Stillinger–Weber potential and the temperature was controlled using Nosé–Hoover thermostat [18].

For the visualisation and characterisation of the simulated structures OVITO visualisation tool [19] is used. Using polyhedral template matching (PTM) from OVITO the structural analysis is made. We also developed our own software for analysing the grain boundary thickness, the grain orientation, and the bond order of atoms. For the classification of local atomic environments (LAEs), we use SOAP [20–22] program from DScribe 1.2 package. The reduction of the LAEs is made using an algorithm that forms groups of LAEs using the given similarity measure and a cutoff value for considering two structures similar enough to categorise being the same.

The rest of the paper is organised as follows. The methods used in the study are presented in section 2. In section 3 we analyse the grain and grain boundary structures of the poly-Si films produced by the molecular dynamics technique [8]. Then we study the grain orientation distribution, the distribution of the thickness of the grain boundaries, and the effects of deposition temperature and post-annealing on them. Finally, we classify and analyse the local environment of atoms in different parts of the poly-Si film. These results form a necessary basis for research into the electrical properties of poly-Si, although this paper does not directly discuss these properties. Finally, we conclude the report with a summary of our key findings.

2. Structure of polycrystalline silicon films

Using the PTM algorithm of OVITO [19, 23] we analyse the structures of the poly-Si films obtained by LAMMPS-simulated deposition. With PTM we can identify different crystal structures. The crystal structures we found were the cubic diamond and the hexagonal diamond structures. Everything else is considered as consisting of atoms that are in a disordered phase before poly-Si growth begins. These are the atoms that are between grains in the grain boundaries and the surface atoms.

Each simulated deposition is a special case, but in this work, we also look for general properties of poly-Si by looking at a large set of simulations. Figure 1 outlines the different stages of poly-Si growth in terms of the relative amount of the crystalline structure and the amorphous structure in different parts of the deposited films. These stages can be seen in the final poly-Si thin film. During the deposition, there is a thin layer of a-Si on the top of the film.

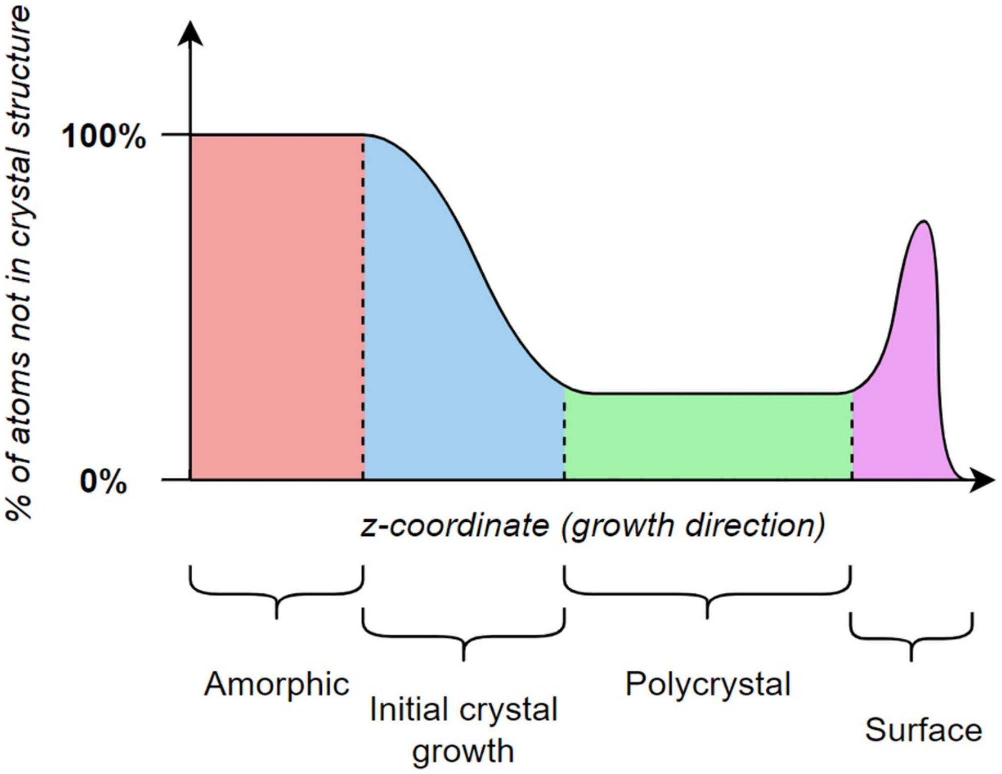

Figure 1. Schematic overview of how our final grown poly-Si film typically looks like. The substrate is on the left and the growth front on the right (the horizontal axis is along the growth direrction). The initial substrate is amorphic (red). At some point, crystals startforming and growing (blue), untill they saturate the simulation box area (green) and we have relatively stable section of poly-Si, where the portion of grains to grain bondaries does not change (green). When we terminate the growth, the surface shows a sharp peak of noncrystal atoms (purple).

The crystallisation takes place under this thin amorphous layer. The initial growth on the substrate is disordered (red part). Eventually, the first crystal grains start to form, which triggers the formation of grains in other parts of the film too (blue). This leads quickly to full grain saturation at the growth front of the film. Then follows a stabilisation period in the simulation, when the relative proportion of atoms in the grain boundaries stays constant (green). During this period of growth, new grains start forming and some old ones stop growing, but usually, few of the bigger grains do grow throughout the whole simulation cell. At the surface, there is a disordered layer of atoms (purple). Some of the grains have not finished growing fully to the surface. In some cases, the surface is not smooth. There are significant bumps where the grains are and valleys where the grain boundaries are. Similar descriptions of the initial growth modes of poly-Si have also been presented based on experimental investigations [24]. When using a longer simulation time, the average final grain size is expected to increase further, provided that larger simulation cells are used. In this study, however, we focus only on the initial stage of poly-Si growth.

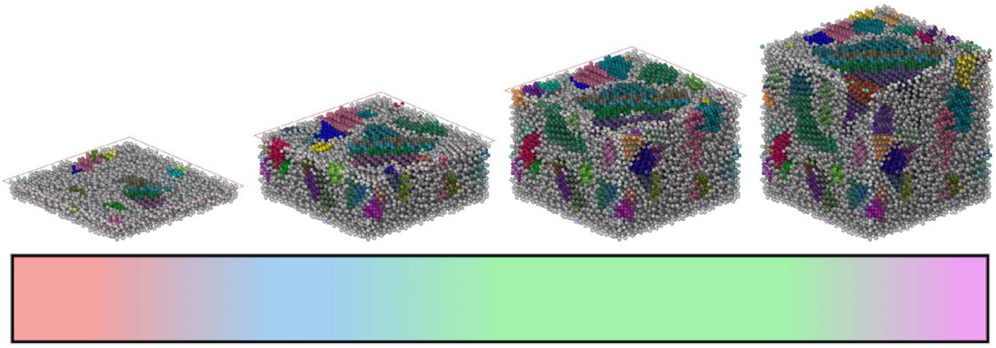

Figure 2. Four cross sections from a typical poly-Si growth (900 K, 100 nm^2 base area). The next image in the series is taken when the poly-Si film is 3 nm thicker than the previous one. These four snapshots represent the poly-Si film at the blue and green parts of figure 1 (the coloured band describes the location in figure 1). Atoms identified as belonging to the diamond structure by PTM are coloured. Starting from left, in the first picture we are in the initial stages of poly-Si growth, where the grains are emerging from various locations. In the second picture, the grains have filled most of the cross-section and have finally saturated it in the third picture. The fourth picture shows how the grains have continued growing.

2.1. Size distribution of the grains

The growth stages seen in figure 1 are visualised in 3-dimensions in figure 2. Starting from the left we have a picture from the beginning of the blue area (figure 1), where the grains are starting to form. The second picture shows how the grains have mostly taken over the whole cross-section area and in the third picture, the grains have fully saturated the whole cross-section. In the fourth picture, the grains have continued to grow and we can see some of the bigger grains from the first picture still present. Some new grains have also started to grow to replace some of the grains that stopped growing.

We annealed two of the systems grown in 900 K for 4 ns in 1350 K. The systems had different growth surface areas, the first one had 100 nm^2 and the second one 400 nm^2. The annealing effect on the sizes of the grains in the system is depicted in figure 3. The smaller system, left graph in the figure, has only a few larger grains initially, while the bigger 400 nm^2 system has a more even distribution of grain sizes. This trend was similar to the other 100 nm^2 systems we had, where in most cases there was always one grain that was considerably bigger than the others. While the biggest grains in the 400 nm^2 system occupy a smaller percentage of the whole system, they do actually still have more atoms in them due to the bigger system having more atoms overall. The increase in cell size allows for more big grains to coexist and grow alongside each others.

During heating, some of the largest grains grow significantly more than others in both cases, both in relative and absolute amounts. When we set the minimum grain size to 30 atoms, the number of grains dropped from 44 to 30, 32% drop, in the smaller 100 nm^2 case and from 333 to 218, 35% drop, in the bigger 400 nm^2 case. Smaller simulation cells seem to lead to a steeper grain size distribution than larger simulation cells.

During annealing, the relative growth of the big grains in the large simulation cell appears to be greater than in the smaller simulation cell. This feels natural because the bigger cell has more energetically unfavourable grains and grain boundaries left. With the annealing, they get overtaken by the bigger grains that have to be energetically more favourable for them to have

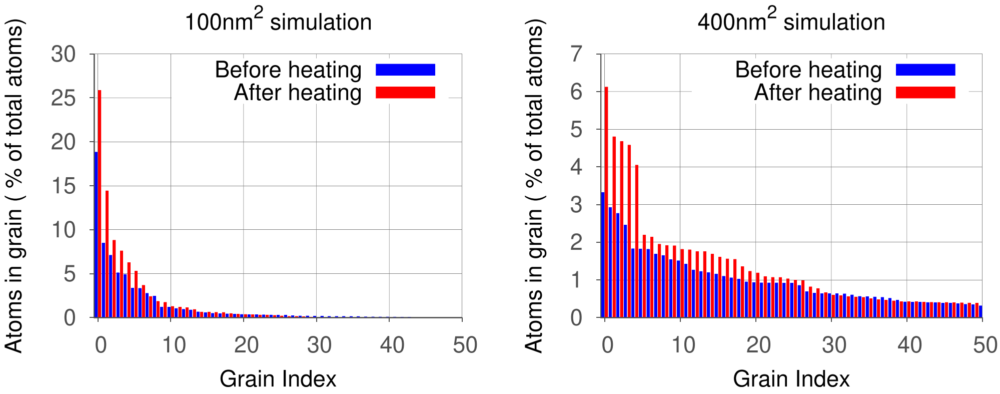

Figure 3. The size of the grains from the 10×10 nm^2 (left) and 20×20 nm^2 (right) poly-Si films. The grain size is given as a percentage of atoms in a grain divided by the total atoms in the poly-Si. Before and after annealing, the grain sizes have been plotted on the vertical axis from largest to smallest. The red bars represent the grain sizes from the post-annealed (1350 K) system and the blue bars from the system before annealing. The annealing increases the size of the bigger grains more than the smaller ones. Typically, a larger system allows larger grains to grow. The distributions of the smallest grains are not shown, the horizontal axis has been cut from both pictures.

grown to that size. The smaller cell is more restrained. Investigating the top of the poly-Si shows that the big grains almost fully cover the poly-Si, so there are very few unfavourable grains and grain boundaries left. The bigger grains still grow, but most of this growth is in the deeper parts of the poly-Si, where there are more energetically unfavourable grain boundaries. The cell size puts a limitation on how thick poly-Si we can grow without periodicity affecting the grains. In our examples, we can already see the effects of this periodicity limiting the growth of the grains when the system is annealed. The 100 nm^2 simulation can only fit one large grain surrounded by smaller grains, while in the 400 nm^2 simulation we have 5 big grains of roughly equal size. This is more noticeable after the annealing, where the five major grains grow significantly more than the other smaller grains.

In determining the resistivity of poly-Si, its grain size distribution is one essential factor. This is because grain boundaries have a higher concentration of electron traps that affect the overall resistivity of poly-Si by trapping charge carriers and forming potential walls for charge carriers through charge trapping. Therefore, since we want to be able to estimate the resistivity of poly-Si in the future, we need to know both the trap density at grain boundaries and the grain boundary size.

2.2. Size distribution of the cross sections of the grains

For comparisons with experiments, it is interesting to look at cross-section images and other grain-related data obtained from our simulations. In figure 4 we have depicted a slice parallel to the growth plain near the surface of the finished growth. The grain boundaries can be seen as black in this image and grains are coloured with different shades of grey. The brighter the shade the bigger the grain is in volume overall in the film. The image is repeated twice in both directions for better visualisation of the side regions of the simulation cell. This cross-section of the initial growth stage can be compared to the SEM image of the surface of a thick poly-Si film shown in [8]. There is a clear difference between these two cross-sections. At the

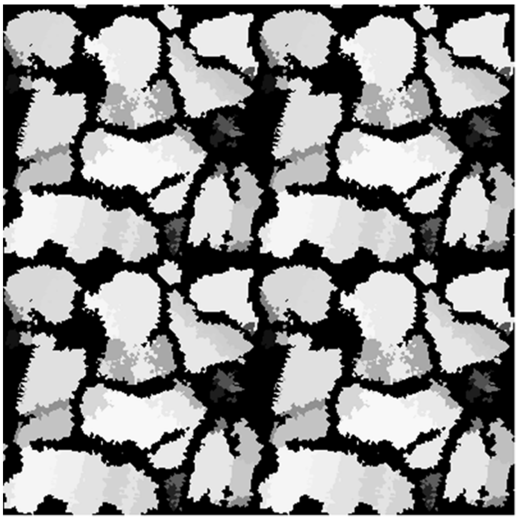

Figure 4. An example of cross-section analyses done for the poly-Si films. The space is divided between all the different atoms in the system. For this cross-section image, if the atom is not in a recognised crystal structure, the pixels near it are coloured black. Pixels near atoms that are in a crystal structure are coloured with different shades of grey to differentiate the grains from each other. The lighter the colour, the bigger the grain. The base area of the simulation cell is 400 nm^2 and the growth temperature is 900 K. (The image is composed of four identical periodic cross-sections to better illustrate the structural property in the side regions of the simulation cell).

initial stage, the crystalline seeds have just met each other and have irregular cross sections on the nm scale, while on the scale of hundreds of nanometers, the cross sections on the surface of the thick poly-Si film appear more circular. In figure 4 we can see shades of grey change continuously from one to another. This usually signifies a stacking fault, where there is a thin hexagonal structure. As such, the two sides of a stacking fault are treated as separate grains, because their orientation in relation to the z-axis, the growth direction, is different.

We can identify in the simulation cell 48 different grains (different shades of grey inside the crystalline islands), but they are grouped into only 10 islands separated by black grain boundaries. As seen in figure 4 the grains still have many possible growth directions. This means that our deposition rate has been so high that the grains have not yet reached their maximum size which, however, can be obtained by post-annealing the poly-Si film. The grain size and the thickness of the grain boundary are important parameters in adjusting the electrical properties of poly-Si. This is because of the traps for mobile charge carriers that are located within the grain boundaries. The smaller the grains are, the more grain boundaries we have and thus higher trap density in the poly-Si. Thicker grain boundaries similarly increase the trap density in poly-Si.

Similar data as shown in figure 4 were also used to calculate the values in table 1. For each of the systems, we picked a height near the top of the deposited film where poly-Si was not affected by the surface structure. We then took a cross-section snapshot parallel to the surface and analysed the grain and grain boundary data from there. Here the different shades of gray are for differentiating the grains from each other, with the brightest shade being the largest grain. Since the growth of poly-Si is a random process, there is a large variation between some data points.

Table 1. table of grain-related data at a cross-section near the surface of the poly-Si film. A, B, and C are different simulations using the same deposition parameters making the statistical variation in the results visible. The first column shows the deposition temperature, the base area of the simulation cell, and whether the poly-Si film is post-annealed or not. The last column shows the relative proportion of atoms in the grain boundaries.

		Grain cross section		
Prepared poly-Si	Grains	Average Size	Biggest	Grain Boundary %
700 K 100 nm^2	15	5.03 nm^2	12.6 nm^2	24.5%
A 800 K 100 nm^2	23	2.85 nm^2	13.3 nm^2	34.5%
B 800 K 100 nm^2	15	5.56 nm^2	16.4 nm^2	16.0%
C 800 K 100 nm^2	26	2.47 nm^2	7.59 nm^2	35.7%
A 900 K 100 nm^2	23	3.01 nm^2	9.65 nm^2	30.7%
B 900 K 100 nm^2	6	12.9 nm^2	39.5 nm^2	21.7%
C 900 K 100 nm^2	12	6.43 nm^2	40.8 nm^2	22.8%
C 900 K 100 nm^2 heated	7	12.7 nm^2	54.6 nm^2	10.9%
900 K 400 nm^2	48	5.26 nm^2	24.6 nm^2	36.0%
900 K 400 nm^2 heated	47	6.08 nm^2	35.5 nm^2	27.8%
900 K 1600 nm^2	193	6.24 nm^2	69.0 nm^2	24.7%

Despite the variations in data values belonging to different deposition simulations, it can be concluded that increasing the growth temperature to 900 K increases both the average grain size and the size of the largest grain. At the same time, the grain boundaries become thinner. Post-annealing has the same overall effect as raising the growth temperature.

2.3. Grain orientations

The electrical and mechanical properties of poly-Si films also depend on the distribution of the crystal orientation of the grains. For the simulated poly-Si films this distribution is shown in an orientation map (figure 5). The map depicts each grain as a dot, that is coloured based on the size of the grain. The location of the dot in the graph tells us which crystal direction of the grain is pointing to the growth direction of the poly-Si film. The three corners in figure 5 correspond to $\langle 100\rangle$, $\langle 110\rangle$ and $\langle 111\rangle$ directions. Si crystal has the cubic symmetry. Any symmetry-wise different orientation in a cubic crystal can be represented by a point on the surface of a sphere, bounded by the great circles of the surface intersecting in the $\langle 100\rangle$, $\langle 110\rangle$, and $\langle 111\rangle$ directions.

Instead of an even distribution, the grain orientations from our simulated depositions of poly-Si show several notable clusterings of grain orientations (figure 5). Most notable clusterings are the $\langle 100\rangle$, $\langle 322\rangle$, $\langle 221\rangle$, $\langle 621\rangle$, $\langle 311\rangle$ and $\langle 110\rangle$ clusters with several bigger grains. Otherwise, there is a fairly even spread of other grain orientations. Next, we compare the grain orientation distribution obtained from the simulations with the x-ray diffraction (XRD) θ–2θ measurement data of a commercial poly-Si film deposited on single crystal Si(100) wafer (figure 6).

One should note that the only diffractions observable in $\theta - 2\theta$ XRD from Si are those whose indexes are all even or odd and of these, those whose diffraction is within the range $2\theta \in (0^\circ, 70^\circ)$ are (111), (220), (131) and (400). Comparing figures 5 and 6 we see that the

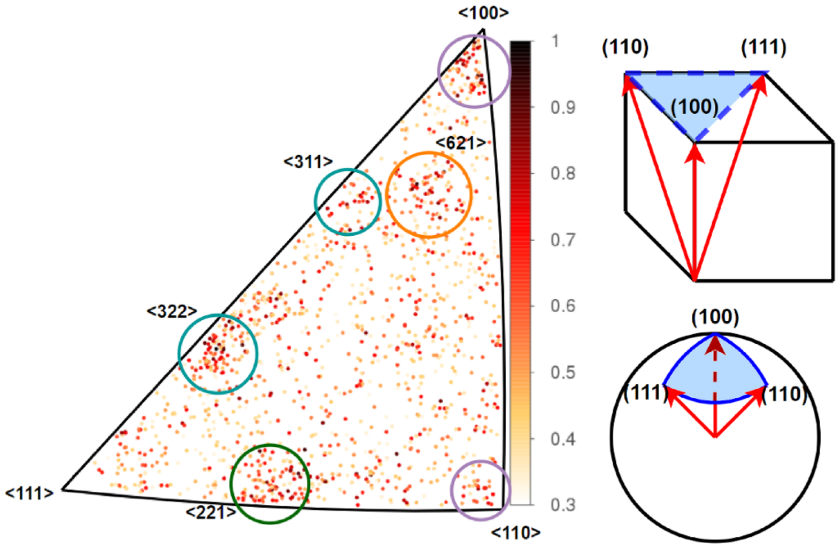

Figure 5. The data from all the simulations (10 simulations, the simulation cell base size from 10×10 nm^2 to 40×40 nm^2). The grains are plotted as a heatmap on the orientation map. The darker the colour the bigger the grain. We have used a logarithmic scale, with 1 corresponding to our biggest 39 757 atom grain. The corners of the triangle correspond to $\langle 100\rangle$, $\langle 110\rangle$ and $\langle 111\rangle$ directions. The schematic pictures on the lower part illustrate the construction of the orientation map as a projection of the irreducible wedge of the directions of the cubic symmetry on the surface of a sphere. We have circled some of the notable clusters of bigger grains and written down an indicative small index direction they are the closest to.

diffractions (220) and (131) shown in figure 6 have also higher probability among the simulated orientations in figure 5, whereas the minor diffraction (111) seen in XRD has very low probability within the simulated orientations. The (131) is the same orientation as (311) and (220) is the same orientation as (110). However, taking into account the intensity ratios of the diffraction peaks of Si powder samples [25], the amount of $\langle 111\rangle$ oriented material in the experiment (figure 6) and simulations (figure 5) correspond well to each other. Namely, since the most intensive diffraction peak in XRD of Si powder samples is (111) (its intensity being more than 3/2 of the second intensive (220) peak), figure 6 actually shows that there is very little $\langle 111\rangle$ oriented material in the commercial poly-Si film. The diffraction (400) in XRD consists of a large component from the Si(100) substrate hiding the same diffraction from the poly-Si layer, if any, making the comparison between the XRD and simulated results in this case impossible. The amorphic bump around $\theta = 20^\circ$ is more intense in poly-Si-covered Si(100) than in Si(100). This is considered to be due to amorphous type grain boundaries in poly-Si.

In summary, the main difference between the XRD from the commercial poly-Si and the orientation distribution from poly-Si from our simulations is that the commercial poly-Si shows a small (111) diffraction peak which is not, according to the orientation map, predicted for the simulated poly-Si films and in the commercial poly-Si the (110) diffraction is the main peak while the (111) and (131) diffractions give only very small contribution whereas in simulated poly-Si the directions $\langle 110\rangle$ and $\langle 311\rangle$ have approximately the same weight.

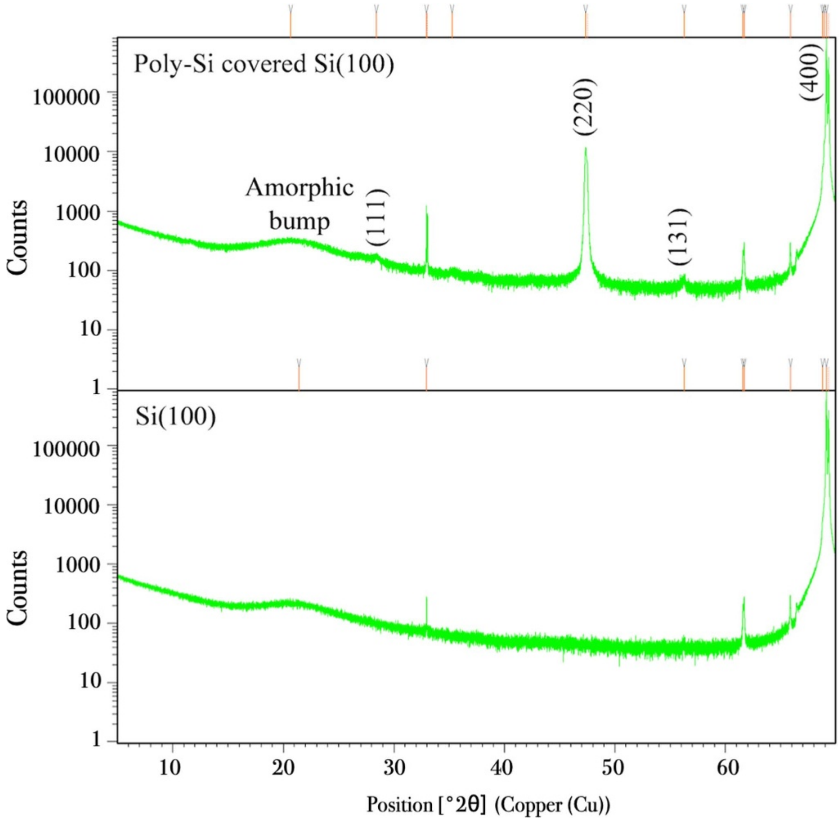

Figure 6. X-ray diffraction (XRD) θ–2θ measurement of a commercial poly-Si covered Si(100) wafer (top) and of a Si(100) wafer (bottom). Peaks without labels are due to the used x-ray equipment.

The observed differences between the XRD results and the orientation distribution of the simulated poly-Si films can be due to several reasons. One of the main reasons could be that the poly-Si film in the commercial wafer is of μm scale whereas the thickness of our simulated poly-Si films is of nm scale. Our simulations illustrate the properties of poly-Si at the beginning of the deposition process, which is known to produce small grains with various forms. In the later stage of the deposition long-shaped grains in the growth direction of the film are formed. The coherently oriented grains in the thicker poly-Si films could have a more limited crystal orientation distribution than that of the grains formed at the beginning of the deposition.

Also, the periodic boundary conditions, perpendicular to the growth direction, and the small size of the simulation cell could have some effect on the results. The base of the simulation cells consists of a few atomic (100) layers of crystalline Si, and on top of that there is a thin layer of a-Si. However, because the size of the crystalline seeds of the grains is small compared with the simulation cell dimensions, it is unlikely that the cell size *per se* would appreciably affect the preferential crystal directions of the grains. For large grains, the periodic boundary conditions impose some restrictions because the base sizes of the simulation cells are multiples of the unit cell of the Si(100) plane. This limitation only comes into effect when the grain size is of the same order of magnitude as the size of the simulation cell, which is a natural point to switch to a larger simulation cell.

With the exception of a few test calculations, the simulations were conducted under fixed base area conditions. This means that if a poly-Si film has a tendency to expand, it can only do so in the direction of growth of the film. The energy-wise release of stress during the growth of such a poly-Si film is most efficiently achieved in grains with the lowest Young's modulus along the growth direction. The Young's moduli of Si, ranging from largest to smallest, are as follows: $E_{111} = 188$ GPa, $E_{110} = 169$ GPa and $E_{100} = 130$ GPa [26], i.e. the same list of directions as the increased probability of finding a principal crystal direction of a grain in the film growth direction (figure 5). However, a more comprehensive investigation of this correlation is left for future studies.

Since the poly-Si growth front is covered by a thin layer of a-Si, the interfacial energy could be an essential quantity to consider in this context. Kioseoglou *et al* [27] have investigated the interface energy between c-Si and a-Si using transmission electron microscopy and molecular dynamics calculations. Their findings indicate that the interfacial energy density is lowest for the $\langle 110 \rangle$ interface and highest for the $\langle 100 \rangle$ interface. However, our results do not align with the interfacial energies reported by Kioseoglou *et al* [27]. This discrepancy may arise from differences in the systems under consideration. Kioseoglou *et al* investigated the crystallisation of a thick a-Si block in contact with c-Si, whereas in our case, there is only a thin a-Si layer in contact with Si crystallites. Additionally, the molecular dynamics simulations employed different potentials. Kioseoglou *et al* [27] utilised the Tersoff potential, whereas we used the Stillinger–Weber potential.

Lu *et al* [28] have made first-principles calculations for Si surfaces (100), (110), (111), and (113). They report that without considering entropy contribution, the relative stability of these Si surfaces from high to low is (111) to (100) and (113) at low temperature, and (100), (113), (110), and (111) at high temperature, assuming the surfaces are ideally reconstructed. The relative stability list of surface orientations at high temperature by Lu *et al* [28] compares well with our list of the same orientations (figure 5), ordered from high to low orientation density.

Huelser *et al* [29] have measured $\theta - 2\theta$ XRD from Si nanoparticles and they show diffraction also for higher 2θ angles ($2\theta \in (70^\circ, 120^\circ)$). They report the following diffraction peaks: (331), (422), (511), (440) and (531).

2.4. Thickness distribution of the grain boundaries

The definition of where the grain ends and where the grain boundary begins is not precise, especially in the case of thick grain boundaries where the edge of the grain boundary contains atoms that have bond orientation and bond coordination that is very similar to the diamond structure. The thickness calculated here depends greatly on how strict we are with the algorithm used to detect the diamond structure, in our case PTM.

Due to the nature of the shape of the grain boundaries in our system, we were not able to separate the grain boundary region into different distinct grain boundaries between different grains. This is why we defined the grain boundary thickness on an atom basis. For each atom in the grain boundary region, we define the thickness of the grain boundary at that location. The algorithm estimates the thickness by finding the closest atom in a grain from one side of the grain boundary and then finding a counterpart from the other side of the grain boundary. The distance between these two atoms is then taken as the grain boundary thickness at that location. The algorithm is slightly inaccurate in irregular locations like the intersections of multiple grain boundaries or small disordered pockets inside grains, but those regions are rare compared to the more regular grain boundary regions.

We used our algorithm to calculate the grain boundary thickness for each atom location in the region of the system with poly-Si grain boundaries. The behaviour in each of the systems

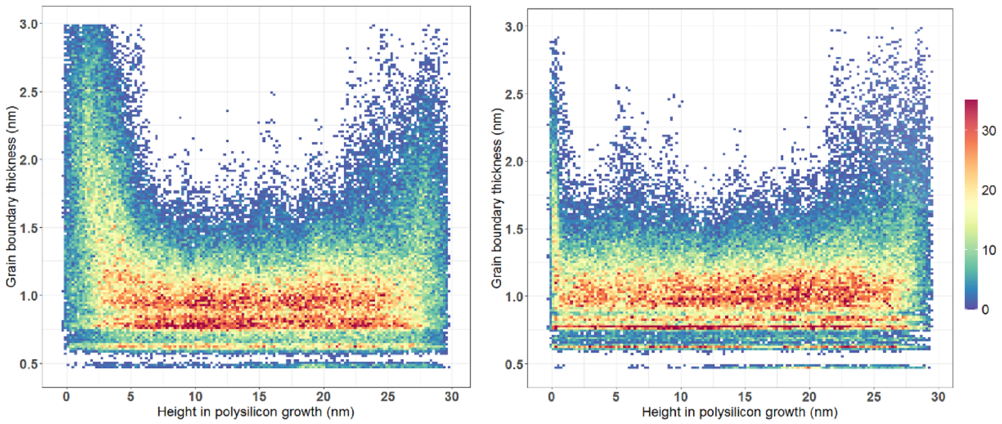

Figure 7. The distribution of the thickness of the grain boundary as a function of the height (from the bottom of the simulation cell) in the film (top) and how the grain boundary thickness changed when the 400 nm^2 900 K system was annealed in 1350 K for 4 ns (bottom). We calculated the thickness of the grain boundary at the location of each atom that is not in a crystal structure and created these heatmaps from that data. The areas below 5 nm and above 25 nm give thicker grain boundaries partly because the poly-Si changes into a-Si at the bottom, whereas at the top we reach an uneven surface with empty gaps.

was roughly the same as seen in figure 7: the range of thicknesses starts out really wide in the beginning of poly-Si formation since the grains are only starting to form. The thickness range settles down quickly to a specific range until we get very close to the surface, where thicker boundaries are more frequent again. Throughout the system, there is a separate peak of thickness a bit below 0.5 nm. This peak is caused by the two atoms thick grain boundaries, which are mostly very orderly, which explains the sharpness and separation of the peak. The peaks for 3, 4, and 5 atoms thick grain boundaries can also be distinguished, but they are wider and blend more into each other.

Si atoms exhibit a high preference for forming four-coordinated bonds, characterised by a tetrahedral bond angle of approximately 109°. This holds true not only for crystalline Si but also for atoms in a-Si and a significant portion of the atoms located at grain boundaries in poly-Si. Hence, it is reasonable to assume that the tetrahedrally coordinated Si atom is the main fundamental structural unit within grain boundaries as well. When two misaligned crystalline Si faces are joined together by Si grain boundary, it becomes evident that a single atom thick grain boundary is incapable of achieving this connection in an energetically favourable way. This is due to the fact that a grain boundary atom cannot be positioned precisely (apart from a few special cases) in the tetrahedral arrangement to atoms of the grains on both sides of the grain boundary. To ensure the correct positioning of the nearest neighbours of the atoms at both grain edges, at least a Si dimer is needed to facilitate the correct tetrahedral bonding of atoms at both grain edges.

To provide an illustrative example, let us consider the thinnest grain boundaries between slightly misplaced coplanar grains of the same crystal orientations. The adjacent Si (100), (110), and (111) atomic planes are separated by distances (d) of 0.14 nm, 0.19 nm, and 0.16 nm, respectively (the lattice parameter of Si is 0.54 nm). To accommodate feasible Si dimers between these grains, the grains should be approximately three times the respective plane distances apart, resulting in distances of 0.42 nm, 0.57 nm, and 0.48 nm for the (100),

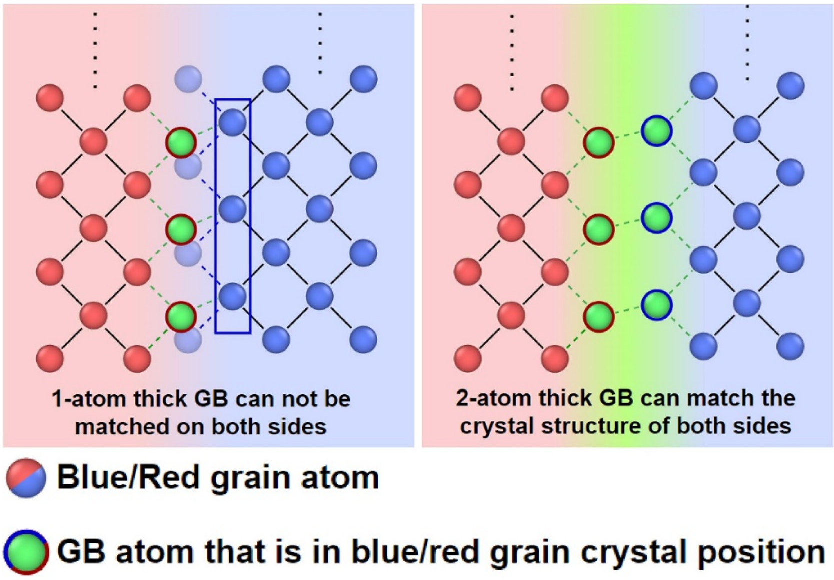

Figure 8. Illustration of a grain boundary forming between two misaligned grains. The red and blue colours represent different grains. Green represents the grain boundary, where the atoms do not have the diamond structure of silicon. On the left, we show that one atom thick grain boundaries are impossible because the gb-atom would have to match the crystal positions of the red and blue grains. Due to the mismatch, the boxed atoms would also turn into grain boundary atoms because their bonding environment does not match the rest of the blue grain (marked in faint blue). It is illustrated on the right that this is possible at a grain boundary two atoms wide.

(110), and (111) cases, respectively. As a result, the average minimum thickness of the grain boundary in this case is estimated to be 0.49 nm. Considering thicker grain boundaries by adding more Si atoms with multiples of the average d of 0.16 nm, we can derive the four smallest thicknesses for the grain boundaries: 0.49 nm, 0.65 nm, 0.81 nm, and 0.97 nm. These estimated values of grain boundary thicknesses compare well with the results of the simulations seen in figure 9: 0.46 nm, 0.61 nm, 0.79 nm, and 0.95 nm. In figure 8 we illustrate this schematically with two misplaced grains forming a grain boundary. The grains are identified with blue and red colours. We see that the one atom thick grain boundary is impossible in this case, but thicker grain boundaries are possible.

Analysing the width of the peaks in the distribution of grain boundary thicknesses provides additional insight into the structure of grain boundaries. Figure 9 shows that the first two peaks are quite narrow and are relatively similar, whereas the third and fourth peaks are considerably broader. This observation implies that two or three atoms thick grain boundaries have limited structural flexibility compared to thicker grain boundaries. The extra space in thicker grain boundaries allows grains to be joined using many different energetically favorable atomic configurations leading to a larger variation in the thickness of the grain boundary.

In figure 7 we have also compared the effect of heating on the grain boundary thicknesses. Above we have the situation before heating, and below we have the situation after heating. Before the heating, there are a lot of wide grain boundaries throughout the simulation cell, especially at the surface and the beginning of poly-Si growth. After 4 ns of heating at 1350 K however, the situation changes. The thick grain boundaries disappear almost completely from

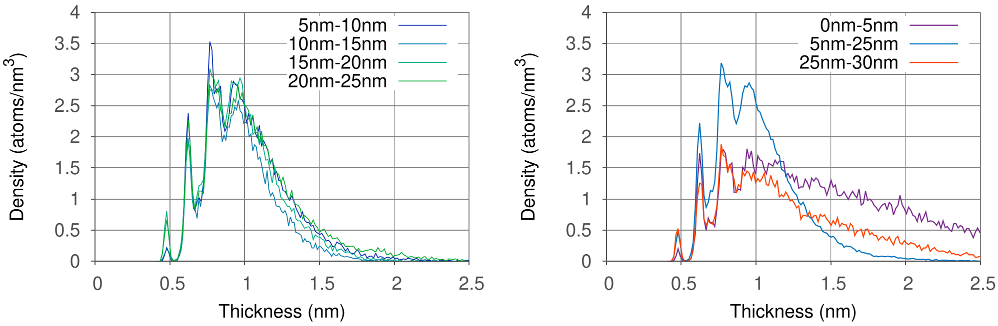

Figure 9. Distribution of grain boundary thicknesses from different depths of the 400 nm^2 poly-Si growth. On the top, we sectioned the middle part (green section in figure 1) of the poly-Si into four different parts. Here we see that the distribution of thicknesses does not really change as the poly-Si growth progresses. On the bottom, we have combined the middle part (blue curve) with the curve from the surface (red) and the start of the poly-Si growth (purple). We see that both the surface and the early growth exhibit more of the thicker grain boundaries.

the bottom of the simulation cell and are only really present at the lowest part, where we had frozen atoms in place for the simulation. The thinner sections are also influenced by the heating. For example, the two atoms thick grain boundaries near $y = 0.5$ nm are much more concentrated on a single value and the same goes for the peaks of what we assume to be 3- and 4-atom thick grain boundaries. Further heating the poly-Si film for 4 ns/8 ns would not alter its structure as noticeably.

As shown in figure 9, the grain boundary thickness distribution is quite unchanged in its main block (5–25 nm, green part in figure 1). The observed small differences can be attributed to just randomness. However, the early deposition region (0–5 nm) and surface region (25–30 nm) display distinctly different distributions of grain boundary thickness. The thickness distribution of the grain boundaries in the early deposition region is as follows: The density of the thinnest grain boundaries is significantly less than that in the main block of poly-Si. When moving to thicker grain boundaries, this difference decreases. Beyond about 1 nm thick grain boundaries the distribution curve starts to decrease, linearly on average. Above about 1.3 nm thick grain boundaries the distribution curve stays above those of the main block and surface region. These characteristics are mainly due to the specific structure of the early depositional region, characterized by crystallites embedded in a-Si. In such cases, the grain boundary data pertains specifically to the distance between crystallites in amorphous material rather than grain boundaries in the conventional sense.

In the surface region, the density of the thinnest grain boundaries is comparable to that in the main block of the poly-Si film. This suggests that the thinnest grain boundaries form at the growth front of poly-Si and their concentration remains unchanged thereafter. The overall linearly decreasing behaviour after approximately 1.3 nm thick grain boundaries is attributed to the special surface structure, which includes a bumpy morphology and crevices (as illustrated in figure 13).

Ding *et al* [9] reported that high resistivity and high electrical linearity of poly-Si films are strongly promoted by stacking faults, Σ_3 twin boundaries as well as Σ_9 grain boundaries contrary to interfaces with random character. Because thick grain boundaries are usually more random type than the thinner ones, it would be beneficial to have more thinner grain boundaries than thick ones.

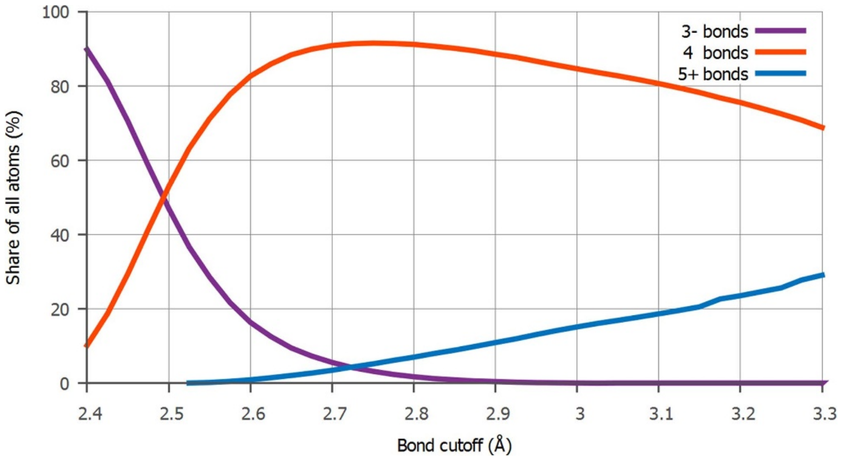

Figure 10. On the x-axis, we have the cutoff radius for bonds. On the y-axis, we have the % of atoms that have this bonding number. This shows how choosing the cutoff radius for bonding can have a significant effect on the results for different bonding numbers. The different curves represent the share of atoms with three or fewer bonds (purple), four bonds (red), and five or more bonds (blue). The chosen LAEs in this example are from the grain boundaries in a poly-Si growth. The base area of the simulation cell is 400 nm^2 and growth temperature was 900 K.

3. Smooth overlap of atomic positions (SOAP)

SOAP is a descriptor for LAEs [20–22]. SOAP descriptor allows us to identify different LAEs from each other through the use of an expansion on local atomic densities. This expansion uses spherical harmonics and radial basis functions, which can for example be polynomial or Gaussian function-based. The radial basis functions are typically weighted so that the atoms far away from the inspected atom are less important. Due to how the descriptor is constructed, it is invariant under rotations, translations, and atom permutations. Unlike some crystal classification tools, SOAP was not built for identifying a specific set of crystal structures, but can instead be used to identify atomic environments [16, 30].

The motivation here was that while using a method where the number of bonds is the number of atoms within some cutoff radius $r_{\mathrm{cut}}^{\mathrm{simple}}$ is very fast, we wanted more control and finesse in the classification of different LAEs. We especially wanted to differentiate all the LAEs with 3 bonds from each others, and all the LAEs with 5 bonds from each others.

The effect of using the simple $r_{\mathrm{cut}}^{\mathrm{simple}}$-method to determine the coordination numbers can be seen in figure 10. In disordered grain boundaries, the silicon-silicon bond distances exhibit significant variation. Therefore, whether a bond exists is not always evident solely from the distance between two atoms. The presence of a bond is contingent upon the overall LAE, which is why relying solely on a cutoff radius is insufficient. To construct the SOAP descriptor for an LAE, the atomic neighbour density is first expanded in a basis composed of spherical harmonics and a set of orthogonal radial basis functions. The coefficients of these radial and spherical basis functions are then combined into a vector, which is called a power spectrum [20, 21]. In practice, this vector is always only the partial power spectrum as we have to limit the size of our basis for computations. This power spectrum was around 1000 components long in this work and it is not very informative for a human in itself. It can, however, be used to accurately compare the similarity of different LAEs to each other, which allows us to identify

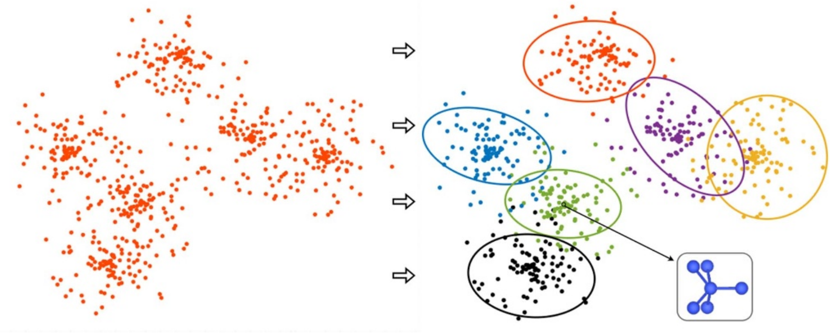

Figure 11. The coarsening of the local atomic environments (LAE) data. The original LAE set is depicted on the left in the picture. This set is searched for clusters of LAEs for which the 'focus point LAEs' are calculated. This set of focus point LAEs is used in further analyses. As an example, one focus point LAE, one type of 5-coordinated Si, is shown in the square box on the right.

the most prevalent LAEs from our simulation. Next, we introduce the measure used to do this grouping based on the power spectrum.

There is a mathematically derived natural distance measure for the power spectrum of two different atomic environments χ_1 and χ_2. If the power spectrum is collected into unit length vectors $\mathbf{p}_{\chi_1}$ and $\mathbf{p}_{\chi_2}$, their distance $\mathbf{d}(\chi_1, \chi_2)$ and similarity $\mathbf{s}(\chi_1, \chi_2)$ according to the derived metric are then given by:

$$\mathbf{d}(\chi_1, \chi_2) = \sqrt{2 - 2\mathbf{p}_{\chi_2} \cdot \mathbf{p}_{\chi_1}} \tag{1}$$

$$\mathbf{s}(\chi_1, \chi_2) = 1 - \sqrt{2 - 2\mathbf{p}_{\chi_2} \cdot \mathbf{p}_{\chi_1}}. \tag{2}$$

This metric gives distance 0, and similarity 1 when the vectors are exactly the same. This can even be expanded to compare structures, groups of atoms, to each other [20–22].

We computed the SOAP power spectrum using DScribe 1.2 for all of our structures [31]. Calculating the spectrum takes several different variables, most notable are the cutoff radius for local environments $r_{\mathrm{cut}}^{\mathrm{SOAP}}$, number of radial basis functions n_{max}, the highest degree of used spherical harmonics l_{max} and the Gaussian smearing factor for the atomic densities σ. On top of that, a weighting function is used to decrease the effect of the atoms further away. Without such a weighting function, these atoms would dominate the descriptor instead of the bonded atom close by to the inspected site.

The amount of LAE data produced by large simulations exceeds the limit of performing reasonable data analysis. In such a case, it is advantageous to make the coarsening of the LAE data. Figure 11 illustrates the coarsening process we use. We took the SOAP power spectrum vectors we obtained from DScribe for our different poly-Si systems. These vectors we used to classify the different local environments present in each system. To do that, we took all the existing environments in the system and started reducing the list to find a small selection of LAEs that describe the system accurately. The reduction was made using an algorithm that forms groups of LAEs using the given similarity measure and a cutoff value for considering two structures similar enough to categorise being the same.

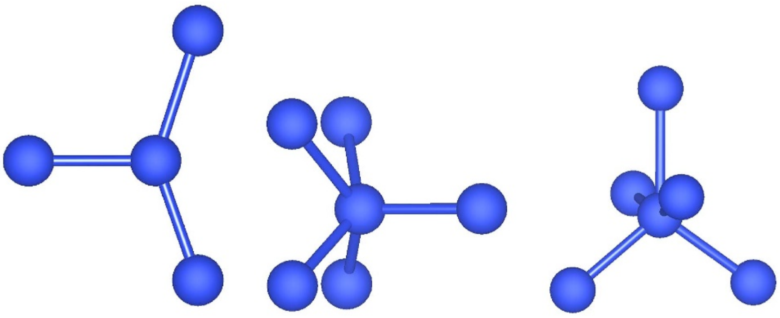

Figure 12. The most common 3-bonded silicon configuration and two 5-bonded silicon configurations. These configurations along with the cubic and hexagonal diamond local environments were the most prominent configurations in all of our poly-Si systems.

We used the similar settings used by [32]. With all of our structures we used $r_{\mathrm{cut}}^{\mathrm{SOAP}} = 3.25$, $n_{\mathrm{max}} = 12$, $l_{\mathrm{max}} = 12$, and $\sigma = 0.5$ to generate the SOAP structures. We note here that the similarity of two different structures changes wildly depending on the used parameters to generate the SOAP power spectrum. Different parameters will also affect the categorising, so it is important to select the parameters carefully. Since we are only interested in the bonding of the silicon atoms, we chose a rather low cutoff range of 3.25 Å for the $r_{\mathrm{cut}}^{\mathrm{SOAP}}$. A study interested also in second neighbours would use a much higher number for the cutoff.

This cutoff range means that there will be multiple categories still corresponding to the 4-coordinated diamond LAE. This is due to the environment being different further away from the initial 4-bonds. We could lower the cutoff range to merge all these similar LAEs, but that would lead to problems with differentiating some other LAEs, especially the higher coordinated silicon environments that can have slightly longer bond lengths.

The size of the radial and rotational basis sets was more of a practical matter, as they affected the resulting file sizes greatly, and increasing them past a certain point did not seem to provide much benefit. Again, too low values though would lead to unexpected behaviour and troubles with telling different LAEs apart from each other.

The found different LAEs could be roughly classified into several different categories: the standard 4-coordinated silicon environments from hexagonal and cubic diamond structures, variations of the one symmetric 3-coordinated LAE, variations of the 2 commonly appearing 5-coordinated LAEs, and a small selection of messy possibly high coordination LAEs that are hard to classify. We were not able to identify the latter, as they have usually a high number (5+) atoms at around the same distance in a disorderly manner. They were such a small minority of all LAEs that we did not see it to be necessary to categorize them, instead, we excluded them.

Excluding the standard 4-coordinated silicon environment, the most common configurations are visualised in figure 12. All the 3-bonded configurations were variations of the configuration on the left. These variations had the 3-bonds turned inwards symmetrically to various degrees. The middle configuration in the figure is dominantly the most common 5-bonded configuration. Variations commonly had the structure deformed in an asymmetrical manner, with multiple bond angles changed. The rightmost configuration in the figure is the second most common 5-bonded configuration.

We used SOAPs to analyse eight different poly-Si growths. The base of the growth was a square with varying total area. We had multiple 100 nm^2 area growths, one at 700 K, three at 800 K and three at 900 K, and one 400 nm^2 growth in 900 K. The three 100 nm^2 growths had

Table 2. The densities of 3-bonded and 5-bonded atoms using r_{cutoff} and SOAP methods, for comparison the atomic density of Si is 5×10^{22} cm^{-3}. The SOAP results are shown also per grain boundary area. Averaged data from poly-Si growth simulations in temperatures 700 K, 800 K, and 900 K, and in simulation cells of 100 nm^2, and 400 nm^2. For 800 K and 900 K, we have three different poly-Si growths. These growths have been labelled A, B, and C.

	3-bonded (cm^{-3})			5-bonded (cm^{-3})		
Temperature	r_{cut}^{simple} (cm^{-3})	SOAP (cm^{-3})	In GB (cm^{-2})	r_{cut}^{simple} (cm^{-3})	SOAP (cm^{-3})	In GB (cm^{-2})
700 K 100 nm^2	1.59×10^{19}	$\mathbf{3.44 \times 10^{20}}$	4.10×10^{13}	7.35×10^{21}	$\mathbf{2.30 \times 10^{21}}$	2.64×10^{14}
A 800 K 100 nm^2	1.47×10^{19}	$\mathbf{7.20 \times 10^{20}}$	8.72×10^{13}	7.92×10^{21}	$\mathbf{1.93 \times 10^{21}}$	2.34×10^{14}
B 800 K 100 nm^2	1.90×10^{19}	$\mathbf{5.62 \times 10^{20}}$	9.63×10^{13}	6.61×10^{21}	$\mathbf{2.10 \times 10^{21}}$	3.60×10^{14}
C 800 K 100 nm^2	1.57×10^{19}	$\mathbf{4.24 \times 10^{20}}$	4.42×10^{13}	6.87×10^{21}	$\mathbf{3.59 \times 10^{21}}$	3.74×10^{14}
Average 800 K 100 nm^2	$\mathbf{1.66 \times 10^{19}}$	$\mathbf{5.69 \times 10^{20}}$	$\mathbf{7.59 \times 10^{13}}$	$\mathbf{7.13 \times 10^{21}}$	$\mathbf{2.54 \times 10^{21}}$	$\mathbf{3.23 \times 10^{14}}$
A 900 K 100 nm^2	1.98×10^{19}	$\mathbf{2.36 \times 10^{20}}$	2.90×10^{13}	4.35×10^{21}	$\mathbf{1.70 \times 10^{21}}$	1.09×10^{14}
B 900 K 100 nm^2	1.04×10^{19}	$\mathbf{3.43 \times 10^{20}}$	7.12×10^{13}	4.07×10^{21}	$\mathbf{1.28 \times 10^{21}}$	2.66×10^{14}
C 900 K 100 nm^2	2.02×10^{19}	$\mathbf{2.54 \times 10^{20}}$	4.14×10^{13}	4.23×10^{21}	$\mathbf{1.49 \times 10^{21}}$	2.43×10^{14}
Average 900 K 100 nm^2	$\mathbf{1.68 \times 10^{19}}$	$\mathbf{2.78 \times 10^{20}}$	$\mathbf{4.72 \times 10^{13}}$	$\mathbf{4.22 \times 10^{21}}$	$\mathbf{1.48 \times 10^{21}}$	$\mathbf{2.01 \times 10^{14}}$
900 K 400 nm^2	1.40×10^{19}	$\mathbf{3.82 \times 10^{19}}$	7.17×10^{12}	3.27×10^{21}	$\mathbf{1.04 \times 10^{21}}$	1.68×10^{14}
A 900 K 100 nm^2 after heating	1.00×10^{18}	$\mathbf{2.00 \times 10^{18}}$	8.02×10^{12}	1.83×10^{21}	$\mathbf{1.86 \times 10^{21}}$	2.54×10^{14}
900 K 400 nm^2 after heating	2.14×10^{19}	$\mathbf{2.14 \times 10^{19}}$	3.71×10^{12}	2.28×10^{21}	$\mathbf{1.21 \times 10^{21}}$	2.10×10^{14}

roughly equal growth of 10 nm thick poly-Si film. The largest simulation has 400 nm^2 base area and the poly-Si film thickness is 24 nm, and is the primary focus of most of the analysis here due to the larger amount of available data. The 1600 nm^2 area system has 13 nm thick poly-Si film.

Table 2 shows different bonding environments and their average number densities based on our SOAP analysis and a simple cutoff-based bond counter (see figure 10), where the $r_{\text{cut}}^{\text{simple}}$ was 3.0 Å. We used 3.0 Å because lower values would result in a considerable amount of 2-coordinated silicon atoms, which clearly should have an extra bond or two. Further inspection would often reveal that many of these atoms would turn out to be 5+ bonded with long bond lengths. We were especially interested in these miscoordinated (3- and 5-bonded) silicon atoms because they are considered to be responsible for most of the charge carrier traps in the grain boundaries.

In figure 13 we have visualised the location of three and five bonded silicon atoms in our 400 nm^2 simulation. We have removed all the grains from the image so that we can visualise the grain boundaries more clearly. We cut this slab from near the surface of the poly-Si growth, which leaves a small crevice filled with three coordinated atoms near the top of the slab. These atoms were not included in the results presented in the table 2 as we think this kind of crevice is mostly due to the growth speed being much faster in simulations than normal. It would also sway the results significantly, and similar crevices were left out from other simulations too.

The miscoordinated Si atoms in poly-Si are expected to generate electronic states in the energy band gap of Si. The band gap states are able to trap charge carriers and reduce the parasitic surface conductivity at the oxide/semiconductor interface [33]. Based on the results presented in this subsection it is possible to calculate the electronic states associated with the 3- and 5-coordinated Si atoms and evaluate their effect on the resistivity of poly-Si, which is our future research topic.

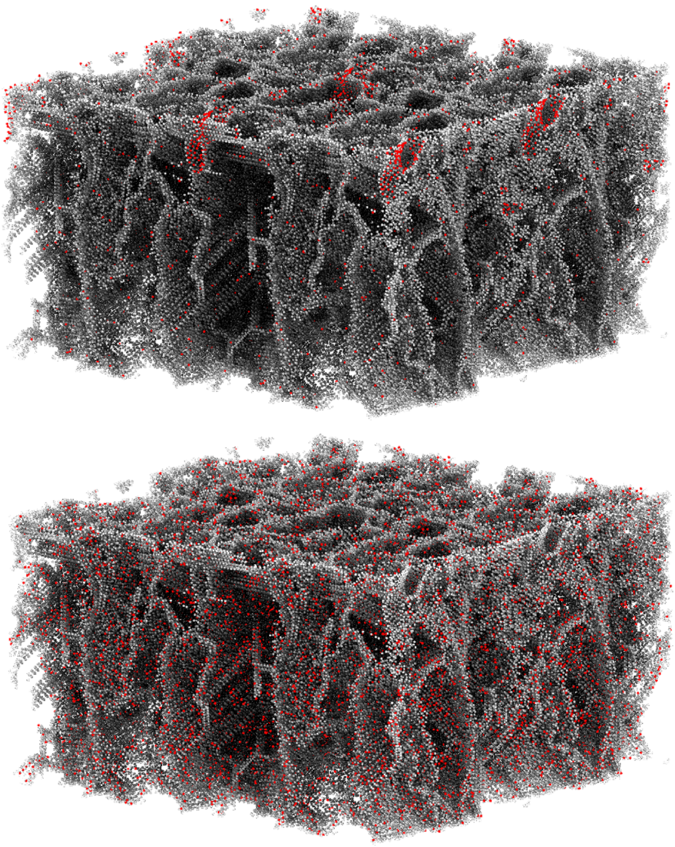

Figure 13. The location of different three(upper) and five(lower) coordinated atoms is highlighted in red in the images. Note the high concentration of three coordinated atoms near the top of the slab. This is due to a small crevice that extends a bit into the poly-Si. This crevice was excluded from coordination analysis because it is an irregularity that highly affects the results.

4. Conclusions

We have studied grains and grain boundaries of poly-Si films obtained by the simulated deposition of poly-Si films based on LAMMPS molecular dynamics simulations [17]. The interaction between atoms was modeled with the Stillinger–Weber potential [18].

The size distribution of the grains seems to be such that there are a few big grains in the simulation cell and a large number of smaller grains of different sizes. Post-annealing increases the size of the large grains, while the smaller grains disappear or do not change much. Considering the crystal orientation of the grains (with respect to the growth direction of the poly-Si film) reveals that there are a few orientations that are more probable than others. The more probable orientations seem to be close to the main crystal directions or the lines between them. A comparison of the simulated orientation distribution with the experimental XRD diffractions from the thick poly-Si film shows similarities, but not a perfect match.

Post-annealing (1350 K) of the simulated poly-Si films makes the grain boundaries considerably thinner. The thickness of grain boundaries is divided into two distinct distributions 'two-atom' thick grain boundaries (thickness a little below 0.5 nm) and '3-atom' thick grain boundaries (a little above 0.7 nm thick). Thicker grain boundaries show more broader distribution.

The determination of the densities of 3-bonded and 5-bonded atoms using the SOAP method shows that the average bulk density of both miscoordinated atomic structures decreases with growth temperature (from 800 K to 900 K). This is further affected by the total area of the grain boundaries within a simulation cell also decreasing with the increasing temperature. The densities behave differently when going from 700 K to 800 K, but we expect this to be due to variance and small sample size.

Data availability statement

The data cannot be made publicly available upon publication because no suitable repository exists for hosting data in this field of study. The data that support the findings of this study are available upon reasonable request from the authors.

Acknowledgments

This work has been supported by Business Finland (Project BEETLES TY 1320731/2021) and Okmetic Oy. The computer resources of the Finnish IT Center for Science (CSC) and the Finnish Computing Competence Infrastructure (FCCI) project (Finland) are acknowledged.

ORCID iDs

Antti Lahti https://orcid.org/0000-0001-7037-4946
Mikael Santonen https://orcid.org/0009-0003-4633-4743
Mikko Miettinen https://orcid.org/0000-0002-5923-6507
Masoud Ebrahimzadeh https://orcid.org/0000-0003-0357-7596
Juha-Pekka Lehtiö https://orcid.org/0000-0002-4762-8554
Pekka Laukkanen https://orcid.org/0000-0003-4220-985X
Marko Punkkinen https://orcid.org/0000-0003-4952-0616
Petriina Paturi https://orcid.org/0000-0002-6240-2801
Antti Kuronen https://orcid.org/0000-0003-0795-8003
Levente Vitos https://orcid.org/0000-0003-2832-3293

References

[1] Rack M, Allibert F and Raskin J-P 2021 Modeling of semiconductor substrates for RF applications: part II-parameter impact on harmonic distortion *IEEE Trans. Electron Devices* **68** 4606–13
[2] Amit I, Englander D, Horvitz D, Sasson Y and Rosenwaks Y 2014 Density and energy distribution of interface states in the grain boundaries of polysilicon nanowire *Nano Lett.* **14** 6190–4
[3] Mueller T, Johlin E and Grossman J C 2014 Origins of hole traps in hydrogenated nanocrystalline and amorphous silicon revealed through machine learning *Phys. Rev.* B **89** 1–7
[4] Ikeda H 2002 Evaluation of grain boundary trap states in polycrystalline-silicon thin-film transistors by mobility and capacitance measurements *J. Appl. Phys.* **91** 4637–45
[5] Kitahara Y, Toriyama S and Sano N 2003 A new grain boundary model for drift-diffusion device simulations in polycrystalline silicon thin-film transistors *Jpn. J. Appl. Phys.* **42** L634–6
[6] Ayres J R 1993 Characterization of trapping states in polycrystalline-silicon thin film transistors by deep level transient spectroscopy *J. Appl. Phys.* **74** 1787–92

[7] Schultz P A 2006 Theory of defect levels and the “band gap problem” in silicon *Phys. Rev. Lett.* **96** 246401

[8] Santonen M *et al* 2024 Polycrystalline silicon, a molecular dynamics study: I. Deposition of polysilicon films *Modelling Simul. Mater. Sci. Eng.* **6** 065025

[9] Ding L, Raskin J P, Lumbeeck G, Schryvers D and Idrissi H 2020 TEM investigation of the role of the polycrystalline-silicon film/substrate interface in high quality radio frequency silicon substrates *Mater. Charact.* **161** 110174

[10] Stokkan G, Song A and Ryningen B 2018 Investigation of the grain boundary character and dislocation density of different types of high performance multicrystalline silicon *Crystals* **8** 341

[11] Ratanaphan S, Yoon Y and Rohrer G S 2014 The five parameter grain boundary character distribution of polycrystalline silicon *J. Mater. Sci.* **49** 4938–45

[12] Mates T 2006 Structure and properties of thin silicon films for solar cells studied by combined atomic force microscopy *PhD Thesis* Charles Uni Prague

[13] Rumler M, Rommel M, Erlekampf J, Azizi M, Geiger T, Bauer A J, Meißner E and Frey L 2012 Characterization of grain boundaries in multicrystalline silicon with high lateral resolution using conductive atomic force microscopy *J. Appl. Phys.* **112** 034909

[14] Orapunt F, Tay L L, Lockwood D J, Baribeau J M, Noël M, Zwinkels J C and O’Leary S K 2016 An amorphous-to-crystalline phase transition within thin silicon films grown by ultra-high-vacuum evaporation and its impact on the optical response *J. Appl. Phys.* **119** 065702

[15] Zhao D and Li Y 2019 Revealing the factors influencing grain boundary segregation of P, As in Si: insights from first-principles *Acta Mater.* **168** 52–62

[16] Deringer V L, Bernstein N, Bartók A P, Cliffe M J, Kerber R N, Marbella L E, Grey C P, Elliott S R and Csányi G 2018 Realistic atomistic structure of amorphous silicon from machine-learning-driven molecular dynamics *J. Phys. Chem. Lett.* **9** 2879–85

[17] Thompson A P *et al* 2022 LAMMPS—a flexible simulation tool for particle-based materials modeling at the atomic, meso and continuum scales *Comput. Phys. Commun.* **271** 108171

[18] Weber T A and Stillinger F H 1985 Local order and structural transitions in amorphous metal-metalloid alloys *Phys. Rev.* B **31** 1954

[19] Stukowski A 2010 Visualization and analysis of atomistic simulation data with OVITO–the Open Visualization Tool *Modelling Simul. Mater. Sci. Eng.* **18** 015012

[20] Bartók A P, Kondor R and Csányi G 2013 On representing chemical environments *Phys. Rev.* B **87** 184115

[21] De S, Bartók A P, Csányi G and Ceriotti M 2016 Comparing molecules and solids across structural and alchemical space *Phys. Chem. Chem. Phys.* **18** 13754–69

[22] Rosenbrock C, Homer E, Csányi G and Hart G 2017 Discovering the building blocks of atomic systems using machine learning: application to grain boundaries *npj Comput. Mater.* **3** 29

[23] Larsen P M, Schmidt S and Schiøtz J 2016 Robust structural identification via polyhedral template matching *Modelling Simul. Mater. Sci. Eng.* **24** 055007

[24] Kočka J *et al* 2004 The physics and technological aspects of the transition from amorphous to microcrystalline and polycrystalline silicon *Phys. Status Solidi* c **1** 1097–114

[25] Ghosh J, Chattopadhyay S K, Meikap A K and Chatterjee S K 2006 Microstructural studies on variation of defect parameters in Zr-Sn alloys and their transition with interchange of solvent and solute in Zr-Ti and Ti-Zr alloy systems by modified Rietveld method and Warren-Averbach method *Bull. Mater. Sci.* **29** 385–90

[26] Hopcroft M, Nix W D and Kenny T W 2010 What is the Young’s modulus of silicon? What is the crystal orientation in a silicon wafer? *J. Microelectromech. Syst.* **19** 229–38

[27] Kioseoglou J, Komninou P, Dimitrakopulos G P, Antoniades I P, Hatalis M K and Karakostas T 2008 Crystallization of amorphous silicon thin films: comparison between experimental and computer simulation results *J. Mater. Sci.* **43** 3976–81

[28] Lu G H, Huang M, Cuma M and Liu F 2005 Relative stability of Si surfaces: a first-principles study *Surf. Sci.* **588** 61–70

[29] Huelser T, Schnurre S M, Wiggers H and Schulz C 2010 Gas-phase synthesis of highly-specific nanoparticles on the pilot-plant scale *Nanotechnology 2010: Advanced Materials, CNTs, Particles, Films and Composites—Technical Proc. 2010 NSTI Nanotechnology Conf. and Expo, (NSTI-Nanotech 2010, 1 November 2014)* pp 330–3

[30] Homer E R, Hensley D M, Rosenbrock C W, Nguyen A H and Hart G L W 2019 Machine-learning informed representations for grain boundary structures *Front. Mater.* **6** 168

[31] Himanen L, Jäger M O J, Morooka E V, Canova F F, Ranawat Y S, Gao D Z, Rinke P and Foster A S 2020 DScribe: library of descriptors for machine learning in materials science *Comput. Phys. Commun.* **247** 106949

[32] Priedeman J L, Rosenbrock C W, Johnson O K and Homer E R 2018 Quantifying and connecting atomic and crystallographic grain boundary structure using local environment representation and dimensionality reduction techniques *Acta Mater.* **161** 431–43

[33] Rack M, Allibert F and Raskin J-P 2021 Modeling of semiconductor substrates for RF applications: part I–static and dynamic physics of carriers and traps *IEEE Trans. Electron Devices* **68** 1–8